Segmentation and radial anisotropy of the deep crustal magmatic system beneath the Cascades arc

Chengxin Jiang[1], Brandon Schmandt[2], Geoffrey A. Abers[3], Eric Kiser[4], Meghan S. Miller[1]

1. Research School of Earth Sciences, The Australian National University, Acton, ACT, Australia

2. Department of Earth and Planetary Sciences, University of New Mexico, Albuquerque, NM, USA

3. Department of Earth and Atmospheric Sciences, Cornell University, Ithaca, NY, USA

4. Department of Geosciences, University of Arizona, Tucson, AZ, USA

Key points:

- Anisotropic Rayleigh and Love wave tomography of the Cascades arc reveals two distinct arc parallel magma reservoirs in mid-lower crust.

- One connecting Mt. Rainier to Mt. Adams (MA) and another Mt. St. Helens (MSH) to Mt. Hood with ~50 km offset at the latitude of MA and MSH.

- They are associated with laterally offset positive radial anisotropy, representing sill complexes with mostly crystallized magma from deep.

Abstract:

Volcanic arcs consist of many distinct vents that are ultimately fueled by the common process of melting in the subduction zone mantle wedge. Seismic imaging of crustal scale magmatic systems can provide insight into how melt is organized in the deep crust and eventually focused beneath distinct vents as it ascends and evolves. Here we investigate the crustal-scale structure beneath a section of the Cascades arc spanning four major stratovolcanoes: Mt. Hood, Mt. St. Helens, Mt. Adams, and Mt. Rainier, based on ambient noise interferometry measurements from 234 seismographs. Simultaneous inversion of Rayleigh and Love wave dispersion better constrain the isotropic shear velocity (Vs) and identify the unusual occurrence of radially anisotropic structures. Isotropic Vs shows two sub-parallel low-Vs zones at ~15-30 km depth with one connecting Mt. Rainier to Mt. Adams, and another connecting Mt. St. Helens to Mt. Hood, which are interpreted as deep crustal magma reservoirs containing up to ~2.5-6% melt, assuming near-equilibrium melt geometry. Negative radial anisotropy is prevalent in this part of the Cascadia margin, but is interrupted by positive radial anisotropy extending vertically beneath Mt. Adams and Mt. Rainier at ~10-30 km depth and weaker positive anisotropy beneath Mt. St. Helens with a west dipping. The positive anisotropy regions are adjacent to rather than co-located with the isotropic low-Vs anomalies. Ascending melt that stalled and mostly crystallized in sills with possible compositional difference from the

country rock may explain the near-average Vs and positive radial anisotropy adjacent to the active deep crustal magma reservoirs.

Plain Language Summary:

Volcanic arcs, a common result of subduction processes, compose a large proportion of active volcanoes in the world and pose significant hazards to our human beings. Seismic tomography measures variations of seismic wave speed in the subsurface, which can then be used to infer important properties of the volcanic systems, such as the distribution and configuration of active melts in the crust. In this study, we use continuous seismic data from 234 seismography in the Cascades arc, and measure the wave speed of two types of surface waves, Rayleigh and Love waves. This allows us to infer not only the averaged shear-wave speed of the subsurface structures, but also its direction dependence, one seismic property known as seismic anisotropy. Our results show two concentrated and arc parallel low-velocity anomalies at 15-30 km depth beneath the arc: one connecting Mt. Rainier to Mt. Adams, and another connecting Mt. St. Helens to Mt. Hood. We interpret these low velocity zones as deep crustal magma reservoirs with up to ~2.5-6% melt. We identify positive radial anisotropy adjacent to the isotropic low-velocity anomalies at similar depth range, and interpret them as sill complexes with mostly crystallized magma extracted from laterally offset deep crustal reservoirs.

Keywords: arc volcano, magmatic reservoir, seismic anisotropy, Mt. St. Helens, sill complex

1. Introduction

Subduction zone plate boundaries extend for hundreds to thousands of kilometers along strike fueling volcanic arcs on the overriding plate. Slab inputs to the mantle that are continuous along strike give rise to discrete volcanoes with variable distance from the plate boundary and along-strike spacing [e.g., *Lee and Wada, 2017; O'Hara et al., 2020*], as well as compositional heterogeneity within and between different volcanoes [e.g., *Wanke et al., 2019; Pitcher and Kent, 2019*]. Heterogeneity also occurs at intermediate scales in which groups of adjacent volcanoes with common geochemical or eruptive characteristics define along-strike segments [*Schmidt et al., 2008; Pitcher and Kent, 2020; O'Hara et al., 2020*]. It is unclear how these aspects of volcanic arc heterogeneity are linked to deep crustal magma reservoirs, which process mantle melt inputs into their eventual volcanic or intrusive products. Magma reservoirs beneath volcanic arcs are thought to span the entire crustal depth range and create long-lived hot zones, although the specific organization of melt accumulations is transient [*Cashman et al., 2017*]. Here, we investigate crustal-scale structure beneath an area including four stratovolcanoes of the Cascades arc extending northward from Mt. Hood to Mt. Rainier (Fig. 1). The two intervening stratovolcanoes, Mt. St. Helens and Mt. Adams, are located at the same along-strike position but separated by about 50 km in distance from the plate boundary. We seek to address the continuity of the deep crustal magma systems beneath these four

stratovolcanoes using insights from anisotropic shear velocity structure.

Recent studies used regional shear velocity (V_S) tomography along with complementary geological constraints to investigate magmatic flux variations along the entire Cascades arc and at local scales. Till et al., [*2019*] show evidence for higher mantle melt flux into the crust beneath the southern to central Cascades compared to the central to northern Cascades where volcanic centers are more spatially isolated. O'Hara et al., [*2020*] find that vent density is correlated with negative Rayleigh phase velocities suggesting upper to middle crustal structural attributes are linked to variable focusing of volcanism along the arc. The present study area, previously referred to as the Columbia segment of the Cascades arc [*Schmidt et al., 2008*] is located near the transition from more distributed vents and higher magmatic flux in the south to more localized vents and lower flux in the north [*O'Hara et al., 2020*].

Local isotropic surface wave tomography has been conducted with subsets of the data used in this study and found that a relatively low Vs zone in the middle to lower crust spans much of the area between Mt. St. Helens, Mt. Adams, and Mt. Rainier [*Flinders and Shen, 2017; Crosbie et al., 2019*]. The absolute V_S of ~3.4-3.6 km/s in this zone is consistent with a small melt fraction but could alternatively be explained by some sub-solidus crustal compositions [*Crosbie et al., 2019*]. It is unclear if this potential deep crustal magma reservoir connects southward to beneath Mt. Hood. Why the volcanic arc hosts two stratovolcanoes at the along-strike position of Mt. St. Helens and Mt. Adams also remains poorly understood [*Bedrosian et al., 2018*]. This study integrates ambient noise interferometry measurements from 234 temporary and permanent seismographs for simultaneous inversion of Rayleigh and Love wave dispersion for a local shear-wave model to gain new insights on the organization of the sub-arc magmatic system. A wide aperture of regional seismic network data combined with dense temporary array data avoids 'edge effects' in the area of interest and provides a continuous view of the magmatic system from Mt. Hood to Mt. Rainier (Fig. 1).

Additionally, this study uses radially anisotropic surface wave tomography to constrain differences in vertically polarized shear velocity (V_{SV}) and horizontally polarized shear velocity (V_{SH}). Recent studies have shown distinctive radial anisotropic structure, with co-located low V_S and V_{SH}>V_{SV}, underlying volcanic systems in arc and intraplate settings with compositionally evolved magmas [*Jaxybulatov et al., 2014; Harmon and Rychert, 2015; Jiang et al., 2018; Lynner et al., 2018*]. These results are consistent with organization of melt into horizontally elongated sill-like volumes. A contrasting result with low V_S and V_{SV}>V_{SH} was found at Piton de la Fournaise, Reunion island, where primitive basalts dominate and more rapid transport through vertical dikes in the crust is hypothesized [*Mordret et al., 2015*]. Many of the recent studies in volcanic fields with evolved compositions focused on voluminous systems including those underlying the Toba caldera [*Jaxybulatov et al., 2014*], Yellowstone and Long Valley calderas [*Jiang et al., 2018*], and the Puna-Altiplano volcanic

field [*Lynner et al., 2018*]. Here, we seek to determine if similar organization of anisotropy is observed at smaller scales beneath four stratovolcanoes of the Cascades arc.

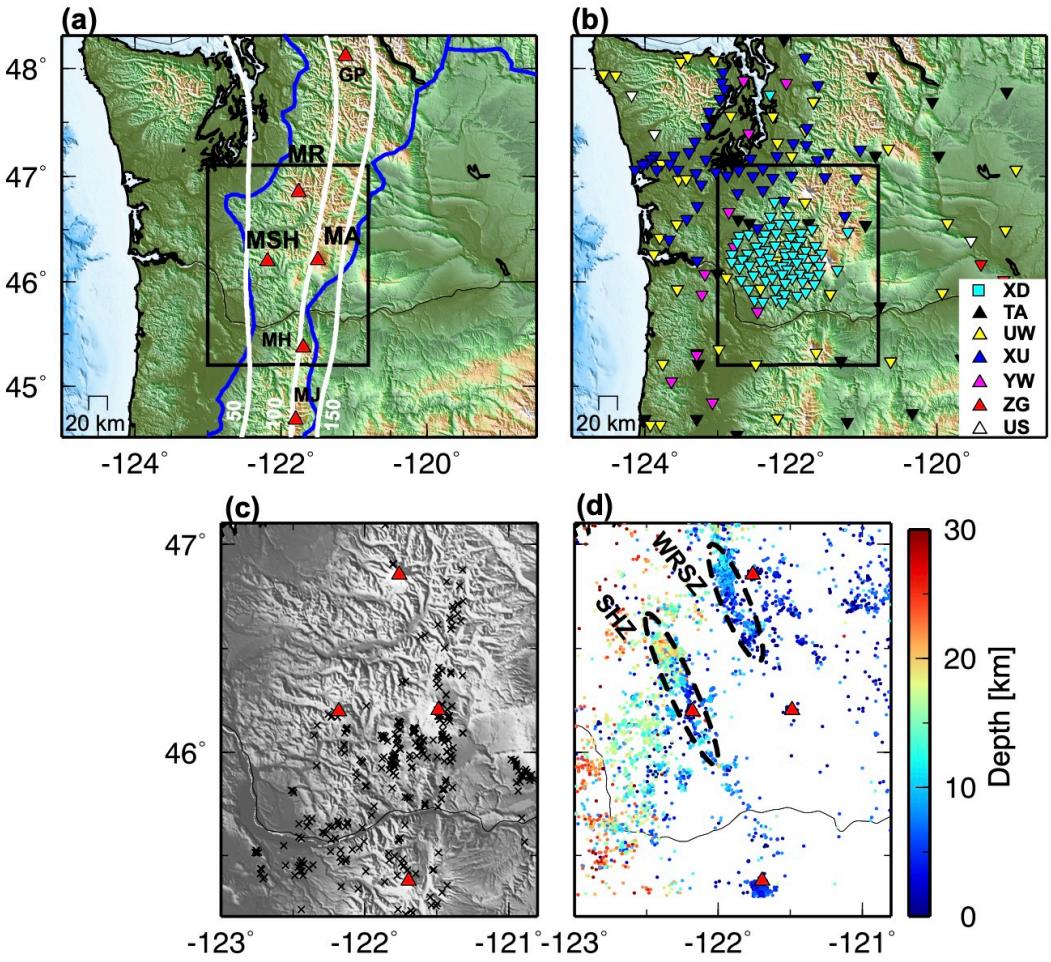

Figure 1. Tectonic context and station map. (a) Tectonic surroundings of the northern Cascades. The red triangles show the major Cascades arc volcanoes, including GP, Glacier Peak; MR, Mount Rainer; MSH, Mount St. Helens; MA, Mount Adam; MH, Mount Hood; MJ, Mount Jefferson. The blue lines denote the boundaries of the Cascades Volcanic Arc. White lines show the 50, 100 and 150 km contours of the Juan de Fuca slab depth from Slab2 [Hayes et al., 2018]. The black box outlines the focus region of this study as shown in Fig. 7-8. (b) Seismic stations used in this study and are color coded by the networks. The dense cyan triangles represent the iMUSH (XD) broadband array. Details of each network can be found in Table 1. (c) Quaternary vents (black crosses;

Hildreth, 2007) in the focused region. (d) Local earthquakes (M1 and above from the Pacific Northwest Seismic Network) in the region color coded by depth. The St. Helens Seismic Zone (SHZ) and Western Rainier Seismic Zone (WRSZ) are indicated with black ellipses [Stanley et al., 1996].

2. Data and Method

2.1 Ambient noise data

Regional coverage is primarily provided by the EarthScope Transportable Array and permanent UW seismic networks (Fig. 1; Supplement Table S1), while temporary denser sampling is primarily provided by the imaging Magma Under St. Helens (iMUSH) project's XD network and the Cascadia Arrays for EarthScope (CAFE) project's XU network. The XD network included 70 broadband seismic stations deployed within 50 km of Mt. St. Helens from June 2014 to August 2016. The XU network from the CAFE project included 60 broadband stations mostly along a transect slightly north of Mt. Rainier, along with some stations more broadly distributed in the forearc and arc. The distribution of all 234 stations is shown in Fig. 1b and network information is given in the Supplementary Materials. Many of the UW, TA, and other regional network stations were present during both dense temporary arrays so there are abundant inter-station paths connecting the dense arrays to the surrounding areas. During data preprocessing, the 3-component continuous data were down-sampled to 1 Hz and the instrument response was removed.

2.2 Ambient noise processing

To process the noise data, we use the python package NoisePy [*Jiang and Denolle, 2020*], which is a high-performance tool designed specifically for large-scale ambient noise seismology. The main noise processing procedures in NoisePy generally follow the conventional workflow of Bensen et al., [*2007*]. First, the data are cut into 30-minute segments with 75% overlap between adjacent windows to increase the signal-to-noise ratio of the stacked cross-correlation functions. To reduce contamination from large transient signals, we removed segments with maximum amplitude >10 times the standard deviation of the amplitude for each day. Second, the mean and trend of the remaining time-series were removed before applying a taper and a 4-pole 2-pass Butter-worth filter from 0.02 - 0.5 Hz. The cross-correlation is then calculated in the frequency domain and a moving average with a window length of 20 samples (~0.011 Hz) is used to smooth the source and receiver spectra. Finally, the cross correlations of the small-time windows are linearly stacked for each station-pair, providing >8,000 stacked CCFs.

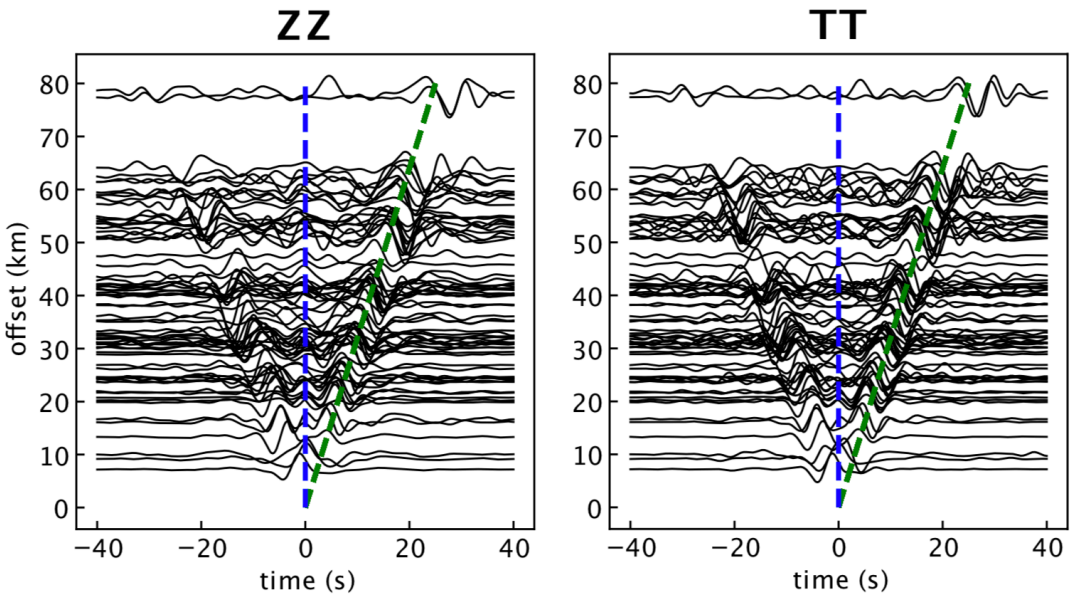

Figure 2. Move-out plot the ZZ and TT components of the correlation tensors between the source station XD.MG05 (marked as a star in Fig. 1b) and the stations within 80 km radius (in the black box of Fig. 1b). The waveforms are filtered at 0.05-0.25 Hz frequency band. The blue dashed lines denote time zero and the green dashed lines show a group velocity of 3.2 km/s.

Figure 2 shows move-out plots for the vertical (ZZ) and transverse (TT) components of the correlation tensors filtered from 0.05-0.25 Hz, with a source station (XD.MG05) located close to Mt. St. Helens and receivers that are synchronous with the XD array. Rayleigh and Love waves travel at similar group velocities of about 3.2 km/s at this broad frequency range around Mt. St. Helens. The move-out plot also displays a weakly asymmetric pattern with the stronger positive lag signals reflecting stronger noise sources from the Pacific Ocean west of the array. Supplementary materials (Fig. S1) include a move-out plot for the same source but with the complete nine-component tensors, which show the Rayleigh and Love wave energies are mostly propagating in plane.

To reduce the effects of inhomogeneous noise source distribution, we average the positive and negative lags of the CCFs to obtain symmetric cross correlations. Frequency-Time analysis (FTAN) was applied to the symmetric Z-Z and T-T components to measure Rayleigh and Love wave dispersion from 2-40 s period. The GDM52 model from Ekström et al., [*2011*] was used as an initial reference for FTAN to guide phase velocity picking at longer periods ($>$ 25 s). Then an updated reference dispersion curve based on the regional average was used to refine phase velocity estimates. Finally, we applied quality control (QC) criteria: 1) signal-to-noise ratio of the CCFs $>$8 [*Bensen et al., 2007*]; 2) interstation dis-

tance > 1.5 wavelengths [*Luo et al., 2015*]. We then inverted for phase velocity maps three times, removing travel times with misfits beyond two standard deviations after the first two inversions. Figure S2 summarizes the final dispersion measurements at each period.

2.3 Surface wave tomography

Dispersion measurements that passed the QC criteria were inverted for 2D phase velocity maps. Least-squares travel time inversions using fixed spatial parameters and regularized with damping and smoothing tend to give poor amplitude resolution [e.g., *Fang et al., 2020*]. To mitigate this challenge, we use a Poisson Voronoi (PV) projection-based tomography method, which projects the original 2D/3D space on a regular grid into low-dimensional subspaces formed by Poisson Voronoi cells. In each subspace, the low-dimension image is efficient to optimize, making it computationally practical to avoid explicit regularization. Fang et al., [*2020*] demonstrated that the inverse problem in the projected subspace is better constrained due to the independence of each subspace. By conducting such inversions many times, each with a random distribution of Voronoi cells, the final solution can be obtained by averaging all solutions from low-dimensional subspaces. The ensemble solution also quantifies model parameter uncertainties.

Phase velocity map inversions were conducted for Rayleigh waves at 3-40 s and Love waves at 3-36 s periods (Fig. S3-4). The 2D model space at each period is parameterized with 350 Voronoi cells. We conducted 50 low-dimensional inversions and used their average and standard deviation as the final model. During each inversion, the travel time wavefield is calculated using the ray-based pyKonal package [*White et al., 2020*]. The wavefield is evaluated on a 0.02°x0.02° grid augmented with 5 times denser sampling near the virtual source and receiver. In each subspace, the low-dimensional problem is optimized with the least-square method without regularization. The phase velocity maps and uncertainties at two example periods of 5 and 18 s are shown in Fig. 3, with the travel time residuals before and after the inversion shown in Supplementary Figure S5.

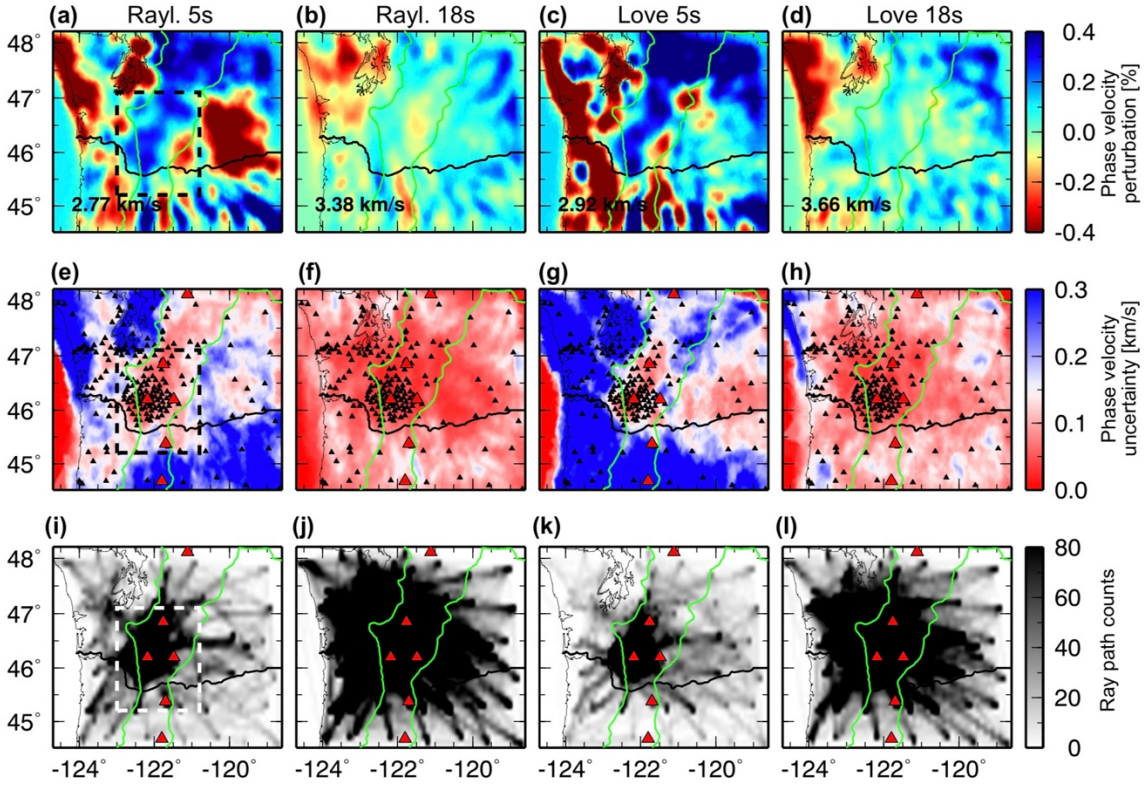

Figure 3. Phase velocity variations related to the regional average and associated uncertainties resulted from the PV-based tomography scheme at two selected periods of 5 and 18 s for Rayleigh and Love waves. The texts in the lower left of (a-d) indicate the regionally averaged phase velocity. The black triangles in (e-h) show the station distribution. The green lines denote the tectonic boundaries of the Cascades volcanic arc. The dashed lines in (a, e, i) outlines the phase velocity maps shown in Figure 5. The red triangles in (e-l) show the major Cascades arc volcanoes.

The example phase velocity maps in Fig. 3 display a series of interesting velocity features in the study region. At a short period of 5 s (Fig. 3a, c), phase velocities are mainly sensitive to shallow crustal structures confined to the uppermost ~8 km. Similar patterns are observed for Rayleigh and Love waves, though Love waves travel slightly faster on average. The most prominent feature is that the Cascades arc exhibits higher phase velocities compared to the surrounding regions. Interestingly, south of 47°N the arc tends to separate into two distinct units with the eastern half showing lower velocities compared to the western half (Fig. 3a,c). The uncertainty maps in Fig. 3e,g reveal that regions of denser path coverage (Fig. 3i, k), such as near Mt. St. Helens, show smaller uncertainties as expected.

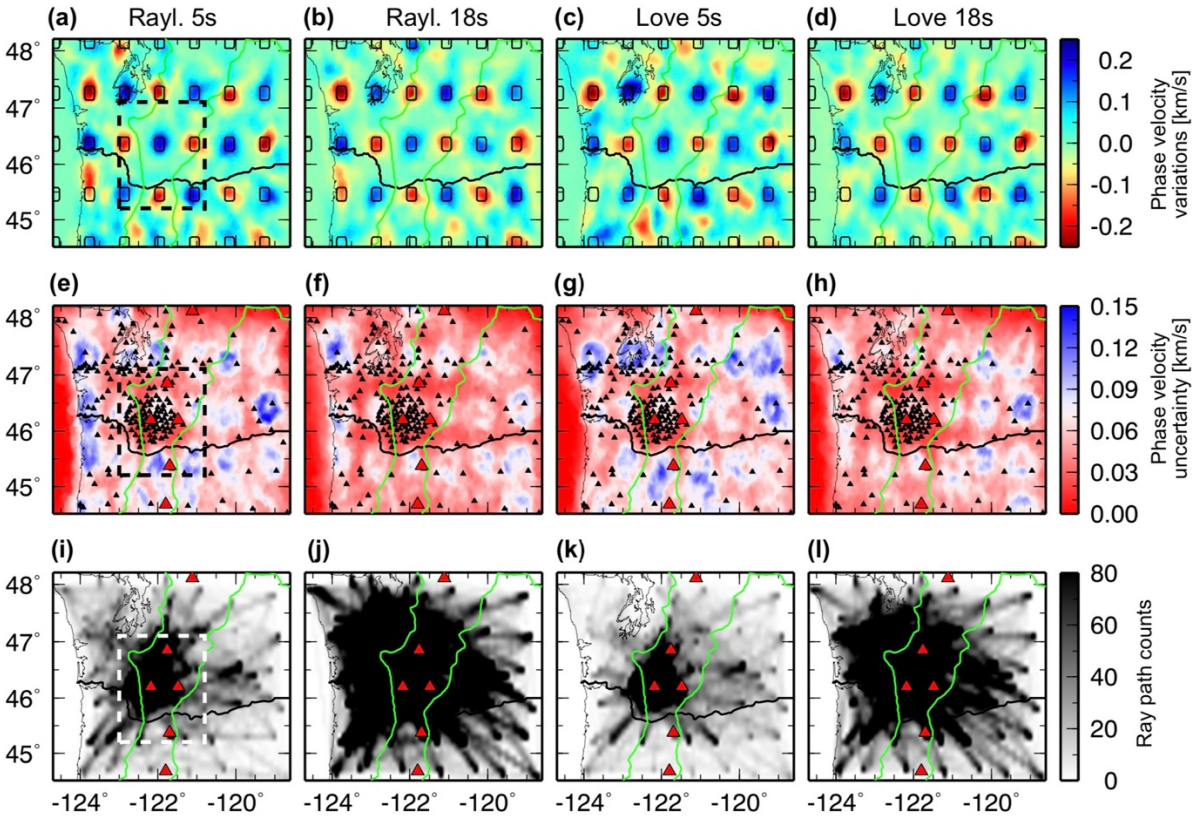

Figure 4. Sensitivity tests for Rayleigh and Love wave phase velocity maps inversion. Inversion result for Rayleigh wave, the associated uncertainty estimates and ray path coverage (on a 0.1°x0.1° grid) at 5 s (a, e, i) and 18 s (b, f, j), respectively. Inversion result for Love wave, the associated uncertainty estimates and ray path coverage at 5 s (c, g, k) and 18 s (d, h, l), respectively. The black boxes in the upper panel denote the 0.25 km/s contour representing the absolute values of the input model relative to the average. The thick dashed lines in (a), (e) and (i) show the focus region of this study. The black triangles in (e-h) show the station distribution. The green lines denote the tectonic boundaries of the Cascades volcanic arc and the red triangles in (e-l) show the major Cascades arc volcanoes.

The phase velocity map at 18 s period (Fig. 3b, d) has smaller and more uniform uncertainties (Fig. 3f, h) because the regional stations provide excellent path coverage across the study area (Fig. 3j, l). Phase velocities at this period reflect a blend of structures at middle crust depths of ~10-25 km. The western portion of the Cascades arc continues to show higher velocities than the east (Fig. 3b, d), although the contrast diminishes in amplitude. The associated uncertainty maps indicate that regions of small uncertainties extend to a much broader

extent compared to those at 5 s period, but the model edges still show larger uncertainties due to diminishing ray coverage (Fig. 3j, l).

2.4 Sensitivity tests

Phase velocity tomography sensitivity tests were conducted to assess model resolution. We input a sparse distribution of spikes rather than the conventional checkerboard model to provide better insights into model reliability [*Rawlinson et al., 2016*]. The model is constructed on the same geographic grid used for the observational data inversion. Spikes are set to have alternating positive and negative amplitude of 10% relative to a background phase velocity of 3 km/s (Fig. 4a). Each spike has a horizontal size of 0.3°x0.3° and is separated by 0.6°. A 2D Gaussian filter with a mean of 0 and standard deviation of 1.5 is applied to smooth the model. Synthetic inter-station phase travel times are calculated using the same station pairs as in the observational tomography with added random Gaussian noise with a standard deviation of 0.5 s, which is close to the traveltime residuals of the tomography for the focused area. Then the inversions are run with the same parameters as in the observational case. Fig. 4 shows the input model and recovered Rayleigh wave phase velocity maps at 5 and 18 s, respectively. Similar results were obtained for Love wave sensitivity tests (Fig. S4). Fig. 4 indicates the PV-based tomography not only recovers the shape of the anomalies but also most of the true amplitude, with a recovery rate up to 80%. Meanwhile, the model does not show strong smearing effects even near edges, which commonly occurs in tomographic inversions relying on regularization. In addition, the PV-based tomography provides reasonable estimates of the model uncertainty, with large values clustered at regions of sparser path coverage.

2.5 Probabilistic method to derive 1D anisotropic profiles

Phase velocity maps are used as inputs for locally 1D V_S inversions, which are combined to form a 3D model. Local dispersion curves were extracted from the phase velocity maps at locations on a 0.1°x0.1° grid for the region located within the black box of Fig. 1a-b. Figure S6 shows the sensitivity kernels of Rayleigh and Love waves as a function of depth across the period range of real data, demonstrating good constraints of Vs to a depth of about 50 km. A Bayesian Markov-Chain Monte Carlo (McMC) inversion method based on Shen et al., [*2013*] was used to invert for local 1D anisotropic V_S profiles on these grid points. The details of this inversion method can be found in Shen et al., [*2013*] and Jiang et al., [*2018*], and are briefly summarized below.

The McMC inversion precedes in three major steps. First, a series of parameters are selected to represent the model space, and the parameter ranges are set to form a prior distribution that spans the potential structural heterogeneity in the region. Second, Markov-chains of candidate models are constructed using parameters randomly selected from the prior distribution. Each Markov-chain evolves in a random walk fashion guided by the Metropolis algorithm [*Mosegaard et al., 1995*] and candidate models are evaluated using the ^{2} misfit

between the predicted dispersion curves and those from the observations, which are computed using subroutines from Computer Programs in Seismology [*Herrmann et al., 2013*]. When an equilibrium in model misfit is attained, a new Markov-chain is formed by randomly sampling the model space again. Finally, a 1D profile and uncertainties are generated using the mean and standard deviation of distribution of the best-fitting models. The McMC inversion method outputs Probability Density Functions (PDFs) for each parameter, allowing further statistical analysis of the model solutions.

We explore the model space through a series of 1-D anisotropic V_S profiles that extend from the surface to 80 km depth and are represented by 13 free parameters. This includes five B-spline coefficients defining a continuous crustal V_S, another five B-spline coefficients form the corresponding radial anisotropy profile in the crust, a parameter denoting the local Moho depth, one isotropic and one anisotropic parameter representing the V_S and associated anisotropy in the upper mantle layer, respectively. The upper mantle layer extends from the local Moho to 80 km depth. Uniform prior distributions are used for all 13 parameters, with the prior distribution of the Moho depth locally centered within ±5 km relative to the reference model of Schmandt et al., [*2015*] (Supplement Table S2). In this study, we define radial anisotropy following equation 1 with Vs representing the average of V_{SV} and V_{SH}. Equation 1 also indicates that positive radial anisotropy means $V_{SH} > V_{SV}$.

$$Aniso = \frac{V_{SH} - V_{SV}}{V_S} \times 100\% \qquad Eq\ 1$$

During the inversion, Vp and density of the 1D profile are scaled to V_S according to the empirical relations 1 and 9 of Brocher et al., [*2005*]. Attenuation effects on surface wave dispersion are corrected following Kanamori et al., [*1977*]. In this study, each 1-D inversion contains 0.7 million iterations and the final average model and uncertainty are calculated from the best 2,000 models. We conducted one synthetic test based on a realistic Vs profile from one example point beneath the Mount St. Helens to demonstrate that our inversion scheme and parameterization adopted here can constrain the depth-dependent isotropic and anisotropic parameters reasonably well (Supplement Fig. S7).

We note that Moho models in the forearc and western Cascades differ among prior surveys as well as between passive and active methods. For example, controlled source P refraction and reflection imaging from Parsons et al., [*1998*] and Kiser et al., [*2016*] indicate ~40 km thick crust between Mt. St. Helens and Mt. Rainier; while Miller et al., [*1997*] estimated a thicker crust, ~48-50 km in about the same location. A summary of Moho estimates from prior controlled source P-wave studies in the region is provided in Supplement Text S1. We choose a reference model of Schmandt et al., [*2015*], which is based on <0.5 Hz Ps receiver functions and reveals ~40 km regional crust, as their dominant sensitivity to low frequency shear velocity contrasts is consistent with our inversion of low frequency surface wave data. In addition, previous studies

indicate that in areas where the Moho is complex, as the case in the wetern Cascades [*Brocher et al., 2003; Bostock, 2013*], methods like teleseismic Ps receiver functions and surface wave dispersion may indicate the center of multi-layer transition or gradient. A more detailed justification for using the reference Moho model of Schmandt et al., [*2015*] is provided in Supplement Text S2.

3. Results

3.1 3D isotropic structure

The isotropic V_S model displays large velocity variations across the study area and throughout the crustal depth range (Fig. 5 and 6), which are well beyond the associated uncertainties (Supplement Fig. S8). . The western half of the volcanic arc is characterized by V_S ~5-10% higher than that of the eastern half at depths <10 km (Fig. 5a, b). The high velocities largely coincide with the Miocene position of the Cascades arc which is located west of the active arc axis at the latitudes in the study area [*Wells and McCaffrey, 2013*]. Exhumed intrusions are prevalent in surface exposures and inferred in the upper crust based on gravity, resistivity, and local earthquake travel time tomography [*Bedrosian et al., 2018; Williams and Finn, 1987; Ulberg et al., 2020*]. The Columbia Basin east of Mt. Adams is characterized by dramatic low velocities at depths <10 km underlain by high velocity anomalies in the lower crust (Fig. 6c). We now focus on the detailed structures beneath the four volcanoes from the surface to the deep crust.

Upper crustal structure varies among the four major volcanoes. In the shallow crust beneath Mt. St. Helens V_S is greater than or similar to the average in the study area, but at depths >10 km a small void of near-neutral velocity anomaly emerges (Fig. 5a-d). Beneath Mt. Rainier V_S is near average at 5 km depth and transitions to ~3% below average by 10 km depth (Fig. 5a-b). In contrast, beneath Mt. Adams and Mt. Hood V_S anomalies of -3 to -6% are found throughout the uppermost 10 km (Fig. 5a-b). The higher upper crustal V_S beneath Mt. St. Helens and near average V_S at 5 km beneath Mt. Rainier may reflect a diluted signal of narrow magmatic systems embedded in the generally higher V_S upper crust of the western Cascades arc. Higher frequency local earthquake and controlled source travel time tomography studies show localized low-velocity anomalies at ~5-10 km depth beneath Mt. St. Helens and Mt. Rainier [*Moran et al., 1999; Ulberg et al., 2020; Kiser et al., 2018*].

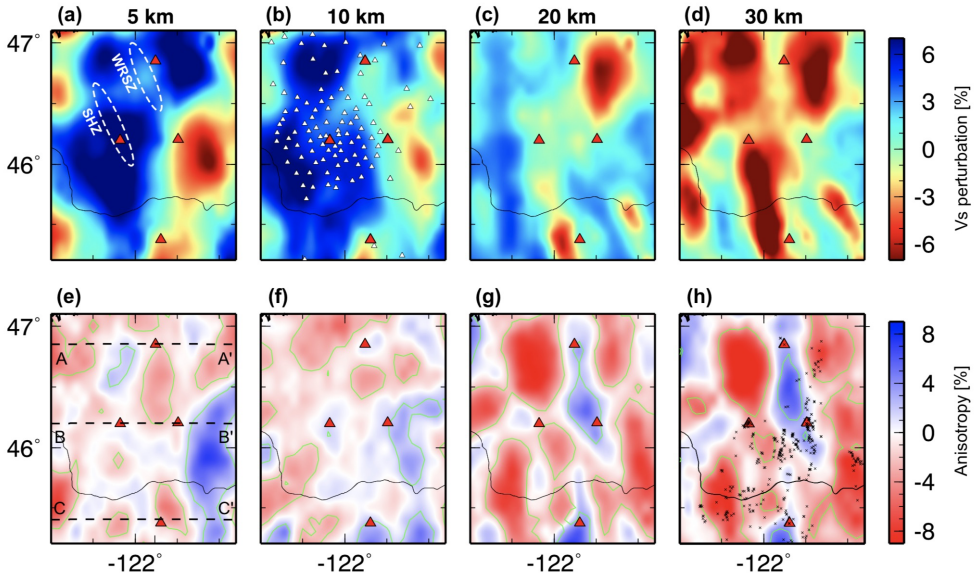

Figure 5. Map views of the 3D anisotropic V_S model plotted at four selected depths of 5, 10, 20 and 30 km, respectively. White dashed ellipses in (a) delineate the WRSZ and SHZ, respectively. White triangles in (b) denote the seismic stations in the target area. The crosses in (h) denote the Quaternary vents [Hildreth, 2007]. The black dashed lines in (e) denote the locations of the cross-section locations shown in Fig. 8. The green lines in (e-h) outline the region of 65% confidence. The four red-filled triangles show the 4 major volcanoes in the region.

In the mid-lower crust (~15-30 km), the most prominent result is that two elongated low velocity zones (LVZs) underlie the arc and span the distance between major stratovolcanoes (Fig. 5c-d): the northern LVZ follows the trend connecting Mt. Rainier to Mt. Adams and the southern LVZ parallels the trend connecting Mt. St. Helens and Mt. Hood. Both LVZs have >5% velocity reductions and their horizontal positions are skewed to one side of each volcano. At 20 km depth (Fig. 5c), the two LVZs display some weak connections where they nearly meet at the latitude of Mt. St. Helens and Mt. Adams. The cross-section view (Fig. 6b) shows that the low velocity anomaly beneath the south side of Mt. St. Helens (3.65-3.71 km/s) dips to the east and is separated from the west-dipping anomaly beneath Mt. Adams by relatively high velocities (3.75-3.8 km/s). The northern LVZ is wider and exhibits slightly lower V_S at 20 km depth (3.3-3.4 km/s), while the southern LVZ is narrower and more elongated sub-parallel to the arc (Fig. 5d and 6).

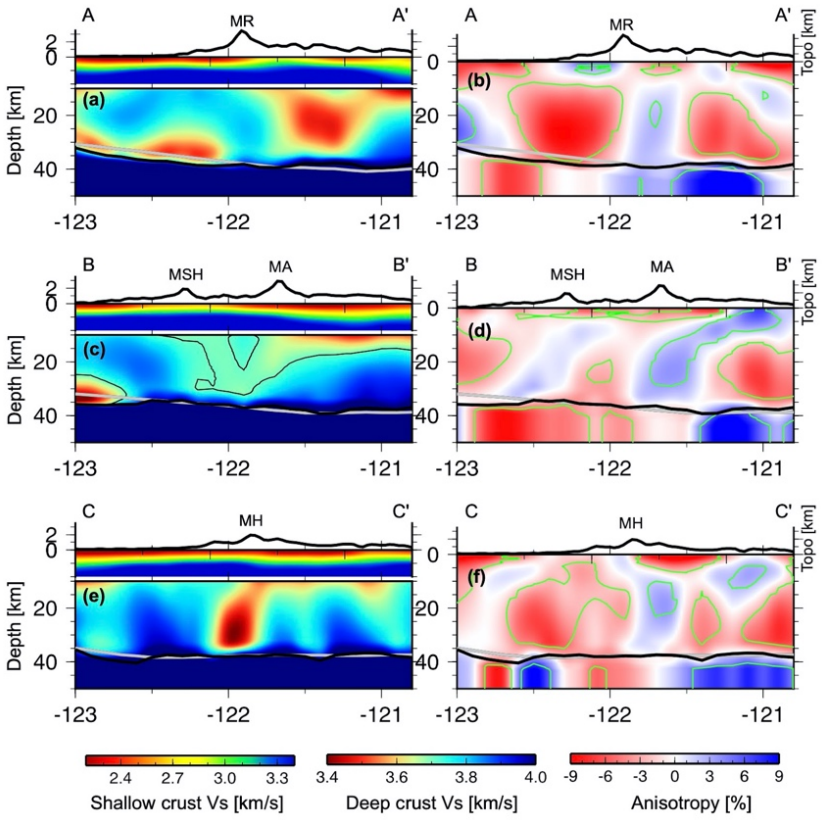

Figure 6. Vertical cross-sections of the 3D isotropic (a, c and e) and anisotropic (b, d and f) V_S model along the three profiles marked in Fig. 5e. The topography variations are plotted on the top of each cross section. The crustal section of the isotropic V_S is broken into two components with different color bars to show the detailed velocity variations. The black lines in (c) show the velocity contour of 3.71 km/s. The thick grey lines illustrate the Moho variation from the reference model of Schmandt et al., [2015] while the thick black lines show the Moho variation from our inversion. The thin green lines in (b, d and f) outline the region of 65% confidence of non-zero radial anisotropy.

Another interesting feature in the isotropic model is the considerably low velocities (3.2-3.3 km/s) in the lowermost crust of the northern forearc region (Fig. 5d), which is also associated with large uncertainties compared to the surrounding areas (Supplement Fig. S8). However, a similar LVZ was mapped by Delph et al. [*2018*] using surface waves and receiver functions to investigate structure near the subduction interface. The LVZ may originate from underthrust sediments with fluids infiltrated from the slab [*Delph et al., 2018*]. Alternatively, Calvert et al. [*2020*] argue that the LVZs are not necessarily subducted sediments but perhaps an over-pressured shear zone within the bottom of the upper

plate.

3.2 Evaluating the significance of radial anisotropy

We firstly show an example location beneath Mt. St. Helens to demonstrate the importance of radial anisotropy parameters to simultaneously fit Rayleigh and Love dispersion. Three scenarios are considered for the 1D V_S inversion: the radially anisotropic parameterization described in section 2.5, an isotropic inversion that maintains 5 b-splines for V_S in the crust but no radial anisotropy parameters, and another isotropic inversion with 10 b-splines in the crust (Fig. 7). The first model using the preferred parameterization has a best ^{2} misfit of 3.2. The second inversion with the anisotropy parameters muted has a best ^{2} misfit of 6.2. The third case tests whether doubling the number of isotropic crustal b-spline parameters could achieve better results without requiring anisotropy, thus it has the same number of parameters compared to that in the first case. Despite the increased number of parameters, the best ^{2} misfit is almost the same as for the isotropic model with only 5 crustal b-splines.

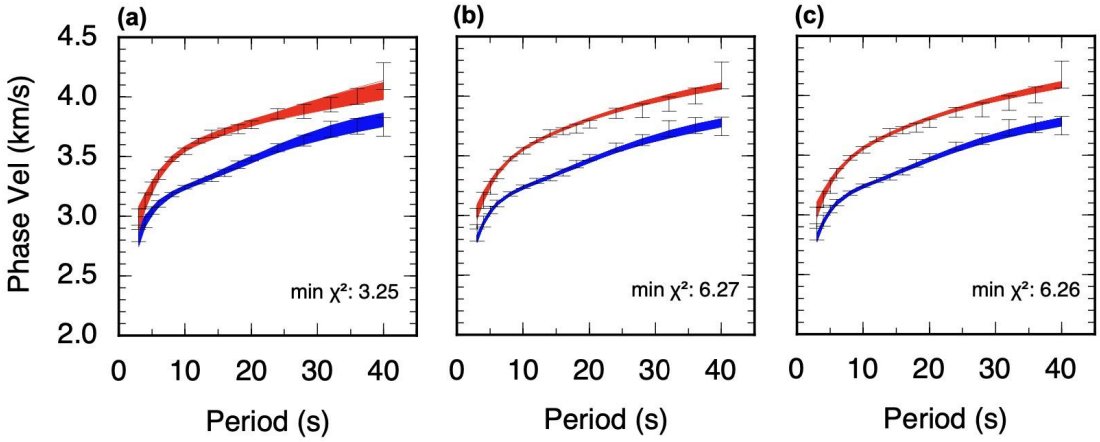

Figure 7. Rayleigh and Love wave dispersion fitting from the Bayesian Markov chain Monte Carlo (MccMC) inversion tests with three different parameterizations. The location is near the center of Mt. St. Helens (46.2°N, -122.2°E). The blue and red lines represent the ensemble of the predicted Rayleigh and Love wave dispersion from the best 2000 models, and the 68% error bars from the 2D tomography. The number in the lower right indicates the minimum 2 misfit from each inversion. (a) is for the inversion with the radially anisotropic parameterization described in section 2.5. (b) is for the inversion using 5 b-splines for V_S in the crust but no radial anisotropy parameters. (c) same as (b) except that 10 b-splines are used in the crust.

Given that the Rayleigh and Love wave dispersion data are much better fit by allowing radial anisotropy parameters in the example test introduced above, our next consideration is whether radial anisotropy parameters are needed in the

depths relevant for the deep crustal magmatic system or just deeper and/or shallower in the model. To do this, we conduct four sets of inversions using the same dispersion data but with different McMC parameterizations. The four parameterizations are: I) isotropic crust and upper mantle; II) isotropic crust and anisotropic upper mantle; III) anisotropic mid-lower crust (splines 3-5) and anisotropic upper mantle; and IV) anisotropic crust (splines 1-5) and upper mantle (Supplement Table S2). The performance of each set of the inversions is evaluated via the ^{2} misfit (Fig. 8).

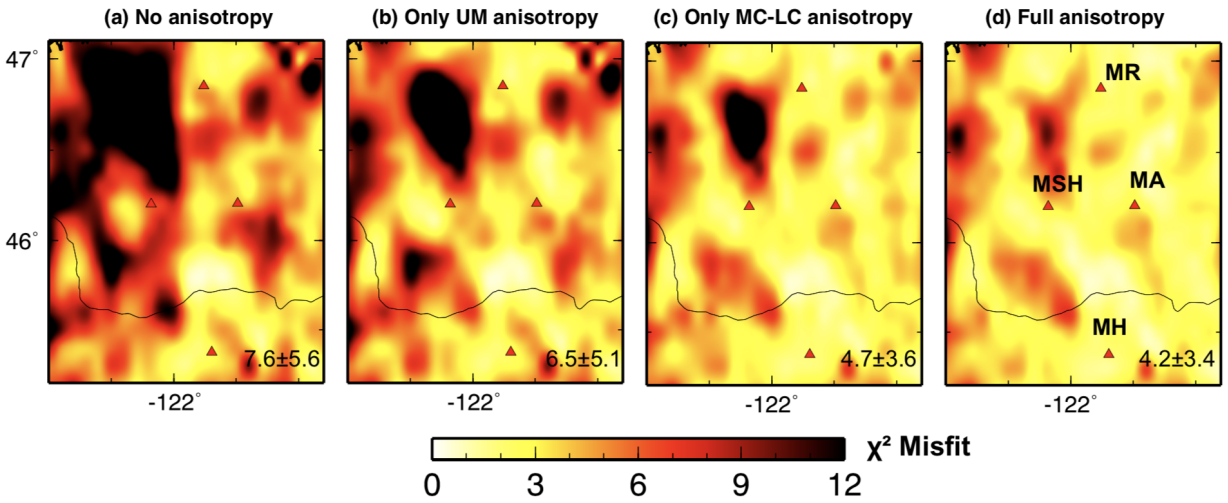

Figure 8. ^{2} misfit maps for the phase velocity measurements across the target region from four sets of inversions using different parameterizations. (a) purely isotropic parameters; (b) only allowing upper mantle (UM) anisotropy; (c) only allowing mid-lower crust (MC-LC) anisotropy and (d) allowing crust and upper mantle anisotropy. The pair of numbers in the lower right of each subplot represents the mean and standard deviation values of each corresponding misfit map. The red triangles mark the volcanoes of Mt. Rainer (MR), Mt. St. Helens (MSH), Mt. Adam (MA) and Mt. Hood (MH), respectively, as labeled in (d).

In general, assuming isotropic crust and upper mantle (model I) poorly fits the observations for most of the study area, with a mean ^{2} misfit of 7.6. Allowing anisotropy only in the upper mantle (model II) slightly leads to a slightly improved mean ^{2} misfit of 6.5. Introduction of anisotropy in the mid-lower crust (model III) results in greater improvement, with mean ^{2} of 4.7. In addition, allowing anisotropy in the shallow crust on top of model III (model IV) further reduces the misfit to ^{2} of 4.2, making it our preferred model (Fig. 7d).

3.3 3D radial anisotropic structure

The anisotropic component of the 3D model provides complementary information to the isotropic V_S structure. In general, the regional crust is characterized by broadly distributed negative anisotropy with an average amplitude of 3-4%

shallower than 10 km depth (Fig. 5e-f) increasing to 7-8% at depth greater than 15 km (Fig. 5g-h). This is consistent with the large-scale western U.S. anisotropic model of Xie et al., [*2015*], in which our study region is the largest area showing negative anisotropy. The rest of the tectonically active western U.S. crust is dominated by positive radial anisotropy [*Moschetti et al., 2010*], which may be focused at middle crustal depths [*Wilgus et al., 2020*]. The exact reason for the negative anisotropic feature in the crust beneath our study region remains to be explored, but indicates subvertical foliations or cracks. Potential mechanisms include the fossil fabrics from the accretionary history of the Cascadia block [*Wells et al., 2014*] and/or the widespread fracture/fault system for vertical fluid migration [*Wells et al., 2017*]. Major volcanic systems are associated with anisotropic features that perturb the regionally prevalent negative anisotropy. We focus on the anomalies in the mid-lower crust as the anisotropy above ~6 km depth is more susceptible to potential bias introduced by the assumed V_P/V_S relation when scaling Vs to Vp for forward modelling as done in section 2.5.

At 10 km depth, moderate positive anisotropy (2-3%) is observed beneath all four volcanoes, coinciding with areas of concentrated low velocity anomalies. At 20-30 km depth, the anomalies beneath Mt. Adams and Mt. Rainier start to merge and form a narrower and stronger feature (4-5%) parallel to the arc. Instead of sitting above the northern LVZ, this anisotropic feature is adjacent (Fig. 5g-h). The positive anisotropy beneath Mt. St. Helens decays in amplitude and dips to the west (Fig. 6d), while the southern LVZ between Mt. St. Helens and Mt. Hood exhibits weak negative anisotropy (-2-3%) at deeper depths.

While the upper mantle exhibits some strong anisotropic anomalies, our one-layer assumption in the inversion and potential complexity in this region make it difficult to interpret. In general, negative anisotropy is more prevalent near the subduction zone and positive anisotropy is more prevalent in the back-arc (Fig. 6d). Studies incorporating longer period data, such as teleseismic surface wave dispersion, could better constrain the upper mantle anisotropic structure so we refrain from detailed interpretation in this study.

4. Discussion

4.1 Segmentation of deep crustal magma reservoirs beneath the Cascades Arc

The two LVZs in the mid-lower crust of the region are among our most important findings. The northern branch is near the previously identified Southern Washington Cascades Conductor (SWCC; Fig. 9b) beneath the three volcanoes of Mt. Rainier, Mt. Adams and Mt. St. Helens. Multiple magnetotelluric studies interpret a conductivity anomaly here as the signal of a complex of subducted sedimentary rocks associated with Siletiza accretion [*Stanley et al., 1987; Bedrosian et al., 2018*]. Alternatively, Hill et al. [*2009*] propose that the SWCC may have a magmatic origin. Based on ambient noise adjoint tomography, Flinders and Shen [*2017*] interpret the SWCC as an extensive region of middle crustal partial melt connecting the three volcanoes (Fig. 9b), consistent

with the conclusion of Hill et al. [*2009*]. Here, we find a partially overlapping LVZ that approximately connects Mt. Adams and Mt. Rainier but becomes subdued between Mt. Rainier and Mt. St. Helens (Fig. 9), which is different from Flinders and Shen [*2017*]. A similar LVZ that trends southeast from Mt. Rainier was imaged by P wave tomography at depths of ~14-23 km, below which the earthquake travel time tomography lacked resolution [*Moran et al., 1999*]. The difference in lateral extent of the LVZ between the new V_S model and the V_S model from Flinders and Shen [*2017*] coincides with an area of positive anisotropy, which means that this part of the LVZ would be more prominent in purely Rayleigh wave tomography rather than the isotropic V_S estimated from Rayleigh and Love waves in this study. The subtle difference of the LVZ between our Vsv and Vs in Figures 9a and 9b might be due to the underestimation of anisotropy at mid-lower crust depth, as shown in the synthetic tests presented in Supplement Fig. S7. We also attribute a greater northeastern extent of the LVZ in this study to the larger number of seismographs, with added coverage within and beyond the arc (Fig. 1b).

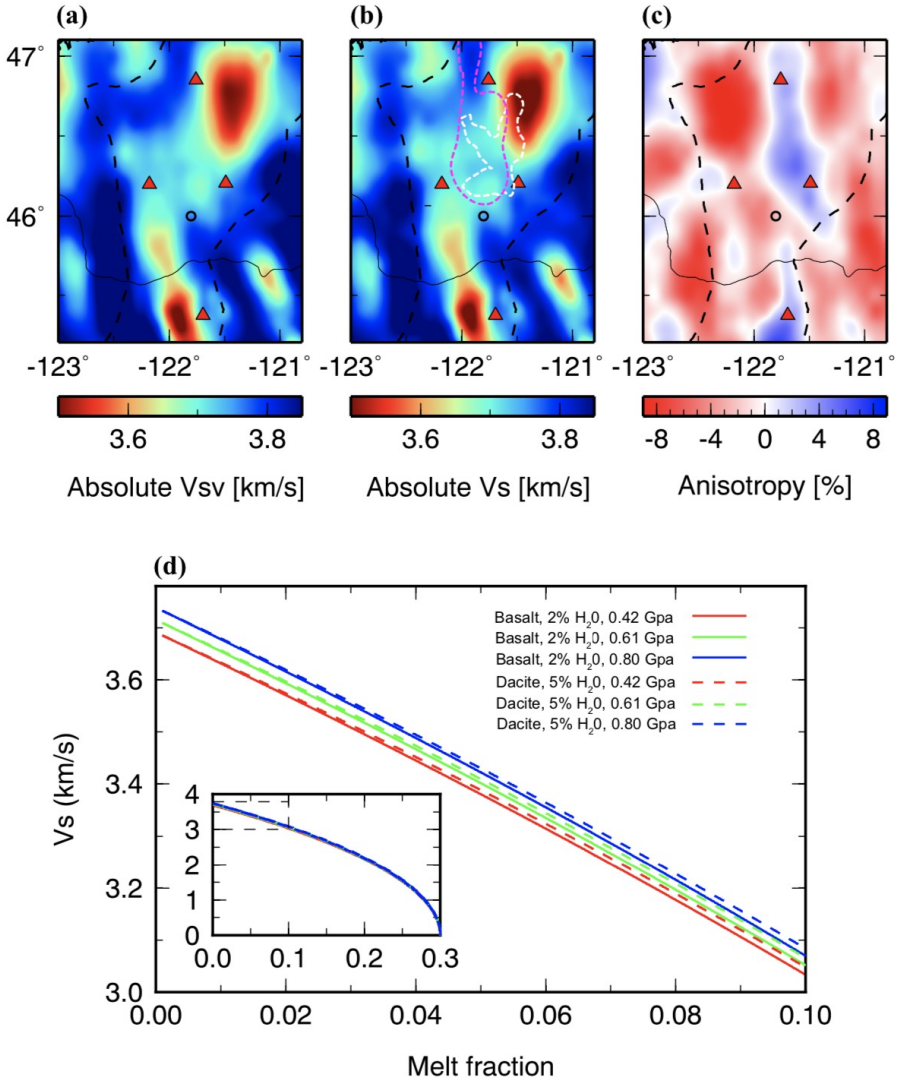

Figure 9. Averaged model at 15-30 km depth range for our study region (a) for absolute V_{SV} (b) for absolute V_S and (c) for radial anisotropy, as well as (d) the derived relationships between melt fraction and the absolute V_S following the approach of Chu et al., [2010] for basalt and dacite compositions color-coded by the H_20 content and crustal pressure conditions. Note this derivation has some assumptions as noted in the section 4.1. Black dashed lines in (a-c) denote the tectonic boundary of Cascades Volcanic Arc, the black circles mark the approximate location of the Indian Heaven Volcanic Field (IH) and the red triangles show the 4 major volcanoes in the region. The white dashed line in (b) approximates the 7% velocity reduction contour at depth of 22 km from Flinders

and Shen [2017]. The magenta dashed line in (b) denotes the location of SWCC [Hill et al., 2009]. The insert in (d) shows the complete range of the relationship with V_S ranging between 0-4 km/s, and the dashed box denotes the zoomed-in portions of the relation shown in the main figure of (d).

Compared to the northern LVZ, the southern one extends between Mt. Hood and Mt. St. Helens and is less studied with prior tomography. Its narrower elongated shape may be more difficult to resolve, and this is the first tomography study to integrate the local array surrounding Mt. St. Helens with wider aperture data south of the Columbia River. Interestingly, Mt. St. Helens and Indian Heaven Volcanic Field are located near the northern periphery of this anomaly (marked in Fig. 9), which shows lower V_S than the area directly between Mt. St. Helens and Mt. Adams (Fig. 9b). This probably explains why previous 2D models or local scale tomography models observe a subtle mid-lower reservoir directly east of Mt. St. Helens (Fig. 10) with absolute V_S that could be reasonably interpreted as sub-solidus crust if it were not beneath an active volcanic arc [e.g., *Kiser et al., 2016, 2018; Crosbie et al., 2019; Ulberg et al., 2020*].

Regional examples of mafic and felsic-to-intermediate compositions are used to evaluate the potential properties of the two inferred mid-lower crustal magma reservoirs. We consider the mean V_S from 15-30 km because that is a well-resolved depth range where the anomalies are most clearly observed (Fig. 9). The average isotropic V_S in that depth range is 3.7 km/s in the area shown in Figure 9 and we consider this an estimate of the host rock properties for the sub-arc magmatic system. An average composition of mafic granulite at 950 °C [e.g., *Rudnick and Fountain, 1995*] produces a good fit using the elastic moduli calculator of Abers et al. [*2016*]. The relationship between V_S and melt fraction was estimated following the approach of Chu et al. [*2010*] with the assumption of effective elastic moduli calculated from a crystalline framework with fluid-saturated pore space, a simplified pressure model and a critical porosity of 30%. Gassman's [*1951*] equations and estimated melt properties for basalt and dacite, with variable water contents, illustrate a plausible range of V_S versus melt fraction relationships. Representative bulk compositions for dacite and basalt were taken from prior studies at Mt. St. Helens [*Wanke et al., 2019*]. The imaged LVZs with 15-30 km isotropic V_S of ~3.45-3.55 km/s correspond to melt fractions of ~2.5-5% for dacitic or basaltic melt with up to 5 wt% water. If instead of the depth-averaged V_S, we consider the minimum observed V_S of ~3.35 km/s at 20 km, then melt fractions up to ~6.5% are predicted. The estimated upper bounds on partial melt in the deep crustal reservoir are lower than estimates for the upper crustal reservoir at Mt. St. Helens, where controlled source P tomography suggests dacite melt fractions up to ~10-12% at ~4-6 km depth [*Kiser et al., 2018*]. We note that different models exist for the Vs versus melt fraction relationship [e.g., *Caricchi et al 2008; Takei, 2002*] and one of the most influential parameters is the assumed geometry of melt-filled pore spaces [*Takei, 2002*]. Aspect ratios much less than 0.1, which are associated with disequilibrium systems, could explain the observed Vs with

lower melt fractions [*Takei, 2002*]. In this study the lowest Vs volumes do not correspond to the areas of strongest anisotropy suggesting that conditions may be close to textural equilibrium. Still, it is not possible to know the relevant pore geometry so the estimates above could be considered upper bounds.

The deep crustal LVZs suggest two magmatic segments based on physical properties that control seismic velocities, such as melt fraction, temperature, and bulk composition. Attempts to cluster Cascades arc volcanoes using geochemical data (major and trace elements, isotopic ratios) provide interesting context for comparison [*Schmidt et al., 2008; Pitcher and Kent, 2019*]. In a recent geochemical clustering study, Mt. St. Helens, Mt. Adams, and Mt. Rainier all reside in the 'Washington' cluster of Pitcher and Kent [*2019*], but the place of Mt. Hood in the clustering is ambiguous. A prior geochemical study placed Mt. Hood, Mt. St. Helens and Mt. Adams in a common 'Columbia' segment and Mt. Rainier in the adjacent 'North' segment [*Schmidt et al., 2008*]. In the new seismic tomography results, Mt. Hood and Mt. St. Helens are spatially linked to the southern LVZ while Mt. Adams and Mt. Rainier are linked to the northern LVZ (Fig. 9a-c). We suggest that geophysical and geochemical clusters differ because deep crustal reservoirs with modest (up to ~6%) melt fractions may not be sufficiently well-mixed to tightly cluster geochemical characteristics. Additionally, common characteristics in deep crustal reservoirs could be obscured by along-strike variations in upper crustal properties that influence the final focusing of magma ascent [e.g, *O'Hara et al., 2020*].

We propose that the unusual arc-perpendicular positioning of Mt. St. Helens and Mt. Adams is linked to the segmentation of the deep crustal magma reservoirs, which are sub-parallel but staggered in east-west position, leaving a small gap between them at the latitude of Mt. St. Helens and Mt. Adams (Fig. 9 and 10). This regional scale organization of sub-arc lower crustal magma reservoirs implies that none of the four stratovolcanoes directly overlie the centroid of their lower crustal magma reservoir. Such lower crustal reservoir offsets are consistent with a recent global compilation indicating that offset reservoir positions become more likely with increasing depth beneath the volcano [*Lerner et al., 2020*]. However, we note that the scenario of offset lower crustal reservoirs that each feed multiple volcanoes poses a challenge for local geophysical imaging studies that intend to image complete subcrustal magmatic systems. Wider aperture imaging studies (e.g., spanning multiple stratovolcanoes) appear valuable for accurately constraining 3D magmatic storage and pathways beneath arc volcanoes.

4.2 Sub-arc anisotropy and implications for magmatic pathways

While our isotropic velocity model helps constrain the melt content in the deep crustal magma reservoirs beneath the Cascades arc, the associated anisotropic features provide some new insights into potential structural fabrics such as organized magma pathways. We image 3-5% positive anisotropy beneath all four volcanic centers at 8-15 km depth range, where shallow magmatic reservoirs are interpreted by higher frequency body wave tomography and magnetotel-

luric imaging (Fig. 10) [*Ulberg et al., 2020; Kiser et al., 2018*]. Positive radial anisotropy is consistent with horizontal layering of heterogeneous seismic velocities [*Jaxybulatov et al., 2014*], and its appearance within the magmatic reservoirs at shallow depths beneath the four volcanoes probably indicates a crystal-rich magma storage zone organized as a sequence of stacked sills. Similar anisotropic features have been observed in the magmatic reservoirs beneath Toba, Long Valley and Yellowstone calderas [*Jaxybulatov et al., 2014; Jiang et al., 2018*]. However, the amplitude of the anisotropy in our study is weaker compared to the large sub-caldera systems (>10%), suggesting smaller reservoirs and less concentrated melt beneath the stratovolcanoes. This is consistent with the ~2.5-5% melt content inferred from the isotropic V_S, compared to ~27% melt estimated for Long Valley [*Flinders and Shen, 2018*] and ~5-32% for Yellowstone using the same assumptions [*Huang et al., 2015; Chu et al., 2010*].

Compared to the similar anisotropic features above 20 km depth, different anisotropic signatures are observed deeper beneath the four volcanoes. Mt. Rainier, Mt. Adams and Mt. Hood all have positive anisotropy extending to mid-lower crust depths, likely representing a continuation of the sill complexes. Such mid-lower crust sill complexes might be common features for arc volcanoes as a similar structure of ~6% positive anisotropy is observed beneath the Costa Rica arc at ~15-30 km depth [*Harmon and Rychert, 2015*]. We note that the connected anisotropic anomaly between Mt. Rainier and Mt. Adams is mostly adjacent to the northern LVZ, indicating greater lower crustal magma storage just east of Mt. Rainier and north of Mt. Adams. The trends of the anisotropy anomalies and the LVZs are almost parallel to the WRSZ and SHZ, suggesting a possible connection between magma migration and the transpressive tectonic strain [*Stanley et al., 1996*]. We suggest that these zones of strain may guide the migration of melt from deep crustal reservoirs into more transient sill complexes beneath specific volcanoes [e.g., *Kohlstedt and Holtzman, 2009*].

Mt. St. Helens is distinctive because its positive radial anisotropy anomaly dips to the west such that the stratovolcano is underlain by a negative anisotropy at >20 km depth, where it overlaps the southern LVZ. The relatively weaker Vs reductions likely indicate less melt directly beneath the volcano, making the relatively weaker anisotropy even more challenging to resolve. This region of lower-crust negative anisotropy is coincident with frequent deep long-period (DLP) events (Fig. 10e-f), whose occurrence is interpreted to reflect the vertical transport of fluids and/or magma [*Nichols et al., 2010; Kiser et al., 2016*]. The negative anisotropy beneath Mt. St. Helens terminates before reaching Mount Hood in the south. Negative radial anisotropy has been previously detected at a mafic volcanic system, Piton de la Fournaise, and interpreted as a set of basaltic dikes responsible for rapid magma transport [*Mordret et al., 2015*]. Similar structure here could suggest more prevalent magma transport through dikes beneath Mt. St. Helens (Fig. 10g).

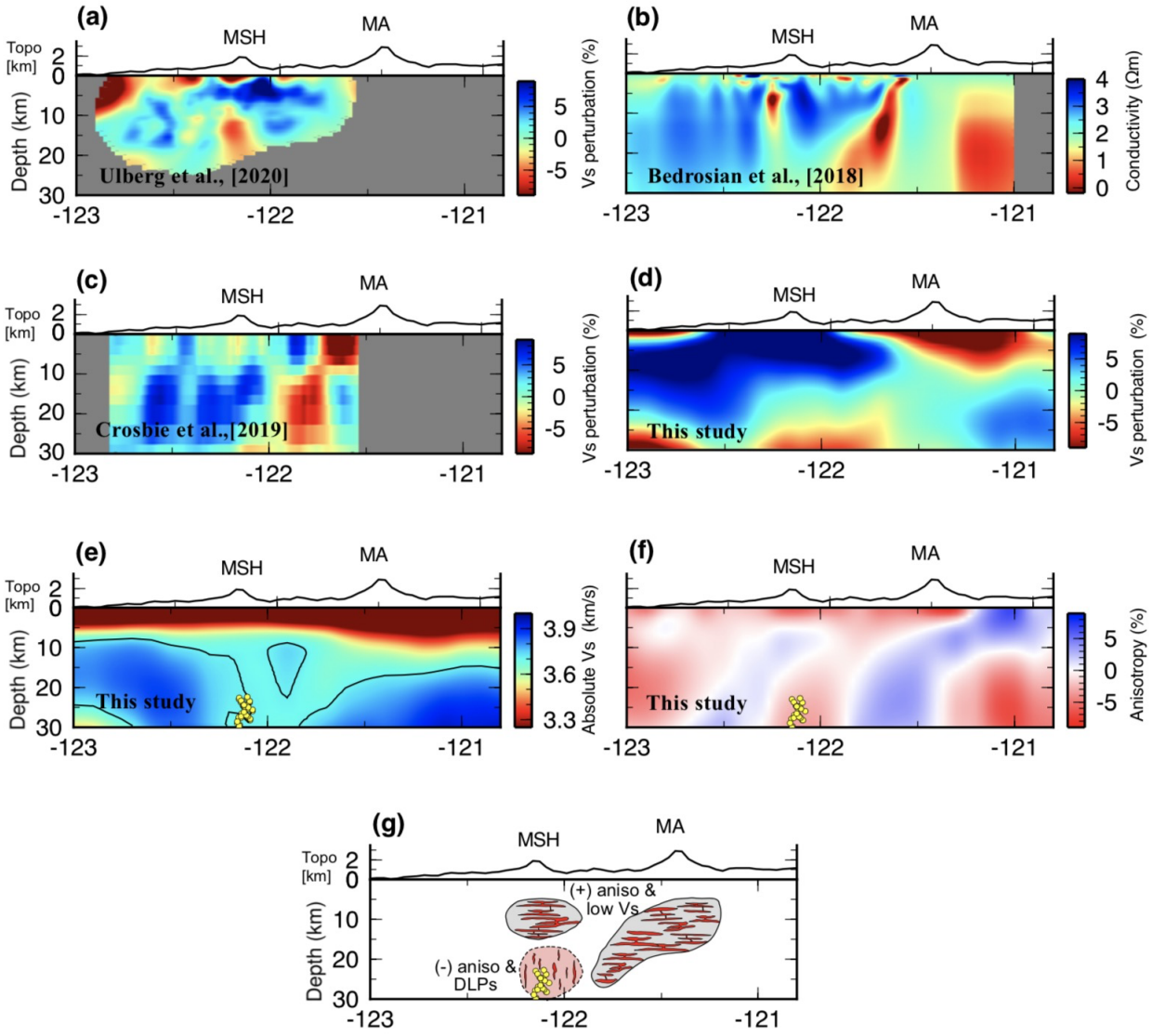

Figure 10. Comparison of three existing geophysical models around Mount St. Helens along with our model along the A-A' profile (a-f) and an interpretative cartoon (g). (a) shows the V_S tomography models from Ulberg et al., [2020]; (b) shows the MT result from Bedrosian et al., [2018]; (c) shows the Vs tomography models from Crosbie et al., [2019]; (d-f) show our new 3D model with the isotropic component plotted in perturbation (d) and absolute V_S (e) and the anisotropic component in (f), respectively. The yellow filled circles in (e-g) denote the deep long-period seismicity (DLPs) from the PNSN catalog. The grey shaded regions in (g) show positive anisotropy and relatively low Vs; while the

red shaded region shows negative anisotropy with vertically aligned DLPs.

5. Conclusions

Ambient seismic noise data from 234 temporary and permanent seismographs in the central to northern Cascades arc were used to image the deep crustal magmatic system. Combined Rayleigh and Love tomography better constrain isotropic Vs and identify radially anisotropic structures. New isotropic V_S images revealed two sub-parallel mid-lower crust magma reservoir segments that span multiple stratovolcanoes. One approximately spans from Mt. Rainier to Mt. Adams and the other from Mt. St. Helens to Mt. Hood. Based on our V_S results, some strict assumptions about magma geometry and basement composition, and previously erupted compositions, ~2.5-6% melt was estimated for the mid-lower crust reservoirs assuming near equilibrium melt geometry. Mid-lower crustal radial anisotropy is important for fitting Rayleigh and Love wave dispersion and estimating isotropic V_S beneath the Cascades arc. Positive radial anisotropy volumes underlie all four volcanoes at 10-20 km depths and are adjacent to the mid-lower crust isotropic LVZs, possibly reflecting the lateral movement of magma from the larger mid-lower crust reservoirs into mostly crystallized sill complexes beneath specific volcanoes. Positive anisotropy extends to the lower crust beneath Mt. Rainier, Mt. Adams and Mt. Hood. Beneath Mt. St. Helens, the positive anisotropy volume dips to the west such that the volcano is underlain by negative anisotropy in the mid-lower crust, suggesting a transition to more dike structures.

The presence of two sub-parallel mid-lower crustal magma reservoirs that are staggered in their east-west positions may help explain why two stratovolcanoes, Mt. St. Helens and Mt. Adams, are present at the same position along strike. Mt. St. Helens lies at the northern end of the southern deep crustal magma reservoir segment while Mt. Adams lies at the southern end of the northern magma reservoir segment. Thus, our results suggest that deep crustal magma reservoirs or hot zones influence the positions of major arc volcanoes, but a given reservoir may fuel multiple stratovolcanoes with horizontal positions that are offset from the centroid of the reservoir.

Acknowledgement

The IRIS Data Management Center was used to access seismic data. A complete list of the seismic network and their full citations are provided in Table S1. The IRIS DMC is supported by the National Science Foundation under Cooperative Support Agreement EAR-1851048. This research was supported by NSF EAR-1554908 and EAR-1950328. Chengxin Jiang acknowledges the financial support from the Discovery Early Career Research Award from the Australian Research Council (DE220100907).

Data Availability Statement

The raw seismic data used in this study are downloaded from IRIS DMC (https://ds.iris.edu/ds/nodes/dmc). Figures were produced us-

ing the Generic Mapping Tools (Wessel et al., 2013). The PV-based surface wave inversion code used in the study is available on GitHub (https://github.com/chengxinjiang/VoroTomo_SW). The inter-station phase velocity measurements from the study will be openly available at Zenodo upon publication.

References

Abers, G. A., & Hacker, B. R. (2016). A MATLAB toolbox and Excel workbook for calculating the densities, seismic wave speeds, and major element composition of minerals and rocks at pressure and temperature. *Geochemistry, Geophysics, Geosystems*, *17*(2), 616-624.

Bedrosian, P. A., Peacock, J. R., Bowles-Martinez, E., Schultz, A., & Hill, G. J. (2018). Crustal inheritance and a top-down control on arc magmatism at Mount St Helens. *Nature Geoscience*, 11(11), 865-870.

Bensen, G. D., Ritzwoller, M. H., Barmin, M. P., Levshin, A. L., Lin, F., Moschetti, M. P., ... & Yang, Y. (2007). Processing seismic ambient noise data to obtain reliable broad-band surface wave dispersion measurements. *Geophysical Journal International*, *169*(3), 1239-1260.

Bostock, M. G. (2013). The Moho in subduction zones. *Tectonophysics*, 609, 547-557.

Brocher, T. M., Parsons, T., Tréhu, A. M., Snelson, C. M., & Fisher, M. A. (2003). Seismic evidence for widespread serpentinized forearc upper mantle along the Cascadia margin. *Geology*, 31(3), 267-270.

Brocher, T. M. (2005). Empirical relations between elastic wavespeeds and density in the Earth's crust. *Bulletin of the seismological Society of America*, *95*(6), 2081-2092.

Calvert, A. J., Bostock, M. G., Savard, G., & Unsworth, M. J. (2020). Cascadia low frequency earthquakes at the base of an overpressured subduction shear zone. *Nature communications*, *11*(1), 1-10.

Caricchi, L., Burlini, L., & Ulmer, P. (2008). Propagation of P and S-waves in magmas with different crystal contents: Insights into the crystallinity of magmatic reservoirs. *Journal of Volcanology and Geothermal Research*, 178(4), 740-750.

Cashman, K. V., Sparks, R. S. J., & Blundy, J. D. (2017). Vertically extensive and unstable magmatic systems: a unified view of igneous processes. *Science*, *355*(6331).

Chu, R., Helmberger, D. V., Sun, D., Jackson, J. M., & Zhu, L. (2010). Mushy magma beneath Yellowstone. *Geophysical Research Letters*, *37*(1).

Crosbie, K. J., Abers, G. A., Mann, M. E., Janiszewski, H. A., Creager, K. C., Ulberg, C. W., & Moran, S. C. (2019). Shear velocity structure from ambient

noise and teleseismic surface wave tomography in the cascades around Mount St. Helens. *Journal of Geophysical Research: Solid Earth*, 124(8), 8358-8375.

Delph, J. R., Levander, A., & Niu, F. (2018). Fluid controls on the heterogeneous seismic characteristics of the Cascadia margin. *Geophysical Research Letters*, *45*(20), 11-021.

Ekström, G. (2011). A global model of Love and Rayleigh surface wave dispersion and anisotropy, 25-250 s. *Geophysical Journal International*, *187*(3), 1668-1686.

Fang, H., Van Der Hilst, R. D., de Hoop, M. V., Kothari, K., Gupta, S., & Dokmanić, I. (2020). Parsimonious seismic tomography with Poisson Voronoi projections: Methodology and validation. *Seismological Research Letters*, 91(1), 343-355.

Flinders, A. F., & Shen, Y. (2017). Seismic evidence for a possible deep crustal hot zone beneath Southwest Washington. *Scientific reports*, 7(1), 1-10.

Gassmann, F. (1951). Elastic waves through a packing of spheres. *Geophysics*, *16*(4), 673-685.

Han, J., Vidale, J. E., Houston, H., Schmidt, D. A., & Creager, K. C. (2018). Deep long-period earthquakes beneath Mount St. Helens: Their relationship to tidal stress, episodic tremor and slip, and regular earthquakes. *Geophysical Research Letters*, *45*(5), 2241-2247.

Harmon, N., & Rychert, C. A. (2015). Seismic imaging of deep crustal melt sills beneath Costa Rica suggests a method for the formation of the Archean continental crust. *Earth and Planetary Science Letters*, *430*, 140-148.

Hayes, G. P., Moore, G. L., Portner, D. E., Hearne, M., Flamme, H., Furtney, M., & Smoczyk, G. M. (2018). Slab2, a comprehensive subduction zone geometry model. *Science*, *362*(6410), 58-61.

Herrmann, R. B. (2013). Computer programs in seismology: An evolving tool for instruction and research. *Seismological Research Letters*, *84*(6), 1081-1088.

Hildreth, W. (2007). *Quaternary magmatism in the Cascades: Geologic perspectives*. US Geological Survey.

Hill, G. J., Caldwell, T. G., Heise, W., Chertkoff, D. G., Bibby, H. M., Burgess, M. K., ... & Cas, R. A. (2009). Distribution of melt beneath Mount St Helens and Mount Adams inferred from magnetotelluric data. *Nature Geoscience*, 2(11), 785-789.

Huang, H. H., Lin, F. C., Schmandt, B., Farrell, J., Smith, R. B., & Tsai, V. C. (2015). The Yellowstone magmatic system from the mantle plume to the upper crust. *Science*, *348*(6236), 773-776.

Jaxybulatov, K., Shapiro, N. M., Koulakov, I., Mordret, A., Landès, M., & Sens-Schönfelder, C. (2014). A large magmatic sill complex beneath the Toba

caldera. *Science*, 346(6209), 617-619.

Jiang, C., Schmandt, B., Farrell, J., Lin, F. C., & Ward, K. M. (2018). Seismically anisotropic magma reservoirs underlying silicic calderas. *Geology*, 46(8), 727-730.

Jiang, C., & Denolle, M. A. (2020). NoisePy: A new high-performance python tool for ambient-noise seismology. *Seismological Research Letters*, *91*(3), 1853-1866.

Kanamori, H., & Anderson, D. L. (1977). Importance of physical dispersion in surface wave and free oscillation problems. *Reviews of Geophysics*, *15*(1), 105-112.

Kiser, E., Palomeras, I., Levander, A., Zelt, C., Harder, S., Schmandt, B., ... & Ulberg, C. (2016). Magma reservoirs from the upper crust to the Moho inferred from high-resolution Vp and Vs models beneath Mount St. Helens, Washington State, USA. *Geology*, 44(6), 411-414.

Kiser, E., Levander, A., Zelt, C., Schmandt, B., & Hansen, S. (2018). Focusing of melt near the top of the Mount St. Helens (USA) magma reservoir and its relationship to major volcanic eruptions. *Geology*, 46(9), 775-778.

Kohlstedt, D. L., & Holtzman, B. K. (2009). Shearing melt out of the Earth: An experimentalist's perspective on the influence of deformation on melt extraction. *Annual Review of Earth and Planetary Sciences*, *37*, 561-593.

Lee, C., & Wada, I. (2017). Clustering of arc volcanoes caused by temperature perturbations in the back-arc mantle. *Nature communications*, *8*(1), 1-9.

Lerner, A. H., O'Hara, D., Karlstrom, L., Ebmeier, S. K., Anderson, K. R., & Hurwitz, S. (2020). The prevalence and significance of offset magma reservoirs at arc volcanoes. *Geophysical Research Letters*, *47*(14), e2020GL087856.

Luo, Y., Yang, Y., Xu, Y., Xu, H., Zhao, K., & Wang, K. (2015). On the limitations of interstation distances in ambient noise tomography. *Geophysical Journal International*, *201*(2), 652-661.

Lynner, C., Beck, S. L., Zandt, G., Porritt, R. W., Lin, F. C., & Eilon, Z. C. (2018). Midcrustal deformation in the Central Andes constrained by radial anisotropy. *Journal of Geophysical Research: Solid Earth*, *123*(6), 4798-4813.

Miller, K. C., Keller, G. R., Gridley, J. M., Luetgert, J. H., Mooney, W. D., & Thybo, H. (1997). Crustal structure along the west flank of the Cascades, western Washington. *Journal of Geophysical Research: Solid Earth*, 102(B8), 17857-17873.

Moran, S. C., Lees, J. M., & Malone, S. D. (1999). P wave crustal velocity structure in the greater Mount Rainier area from local earthquake tomography. *Journal of Geophysical Research: Solid Earth*, *104*(B5), 10775-10786.

Mordret, A., Rivet, D., Landès, M., & Shapiro, N. M. (2015). Three-dimensional shear velocity anisotropic model of Piton de la Fournaise Volcano (La Réunion Island) from ambient seismic noise. *Journal of Geophysical Research: Solid Earth*, 120(1), 406-427.

Mosegaard, K., & Tarantola, A. (1995). Monte Carlo sampling of solutions to inverse problems. *Journal of Geophysical Research: Solid Earth*, *100*(B7), 12431-12447.

Nichols, M. L., Malone, S. D., Moran, S. C., Thelen, W. A., & Vidale, J. E. (2011). Deep long-period earthquakes beneath Washington and Oregon volcanoes. *Journal of Volcanology and Geothermal Research*, *200*(3-4), 116-128.

Moschetti, M. P., Ritzwoller, M. H., Lin, F., & Yang, Y. (2010). Seismic evidence for widespread western-US deep-crustal deformation caused by extension. *Nature*, *464*(7290), 885-889.

O'Hara, D., Karlstrom, L., & Ramsey, D. W. (2020). Time-evolving surface and subsurface signatures of Quaternary volcanism in the Cascades arc. *Geology*, *48*(11), 1088-1093.

Parsons, T., Trehu, A. M., Luetgert, J. H., Miller, K., Kilbride, F., Wells, R. E., ... & Christensen, N. I. (1998). A new view into the Cascadia subduction zone and volcanic arc: Implications for earthquake hazards along the Washington margin. *Geology*, 26(3), 199-202.

Pitcher, B. W., & Kent, A. J. (2019). Statistics and segmentation: Using Big Data to assess Cascades Arc compositional variability. *Geochimica et cosmochimica acta*, *265*, 443-467.

Rawlinson, N., & Spakman, W. (2016). On the use of sensitivity tests in seismic tomography. *Geophysical Journal International*, *205*(2), 1221-1243.

Rudnick, R. L., & Fountain, D. M. (1995). Nature and composition of the continental crust: a lower crustal perspective. *Reviews of geophysics*, *33*(3), 267-309.

Schmandt, B., Lin, F. C., & Karlstrom, K. E. (2015). Distinct crustal isostasy trends east and west of the Rocky Mountain Front. *Geophysical Research Letters*, *42*(23), 10-290.

Schmandt, B., Jiang, C., & Farrell, J. (2019). Seismic perspectives from the western US on magma reservoirs underlying large silicic calderas. *Journal of Volcanology and Geothermal Research*, 384, 158-178.

Schmidt, M. E., Grunder, A. L., & Rowe, M. C. (2008). Segmentation of the Cascade Arc as indicated by Sr and Nd isotopic variation among diverse primitive basalts. *Earth and Planetary Science Letters*, 266(1-2), 166-181.

Shen, W., Ritzwoller, M. H., Schulte-Pelkum, V., & Lin, F. C. (2013). Joint inversion of surface wave dispersion and receiver functions: a Bayesian Monte-Carlo approach. *Geophysical Journal International*, 192(2), 807-836.

Stanley, W. D., Johnson, S. Y., Qamar, A. I., Weaver, C. S., & Williams, J. M. (1996). Tectonics and seismicity of the southern Washington Cascade Range. *Bulletin of the Seismological Society of America*, *86*(1A), 1-18.

Takei, Y. (2002). Effect of pore geometry on VP/VS: From equilibrium geometry to crack. *Journal of Geophysical Research: Solid Earth*, 107(B2), ECV-6.

Till, C. B., Kent, A. J. R., Abers, G. A., Janiszewski, H. A., Gaherty, J. B., & Pitcher, B. W. (2019). The causes of spatiotemporal variations in erupted fluxes and compositions along a volcanic arc. *Nature communications*, *10*(1), 1-12.

Ulberg, C. W., Creager, K. C., Moran, S. C., Abers, G. A., Thelen, W. A., Levander, A., ... & Crosson, R. S. (2020). Local source Vp and Vs tomography in the Mount St. Helens region with the iMUSH broadband array. *Geochemistry, Geophysics, Geosystems*, 21(3), e2019GC008888.

Wanke, M., Clynne, M. A., von Quadt, A., Vennemann, T. W., & Bachmann, O. (2019). Geochemical and petrological diversity of mafic magmas from Mount St. Helens. *Contributions to Mineralogy and Petrology*, 174(1), 10.

Wells, R. E., & McCaffrey, R. (2013). Steady rotation of the Cascade arc. *Geology*, *41*(9), 1027-1030.

Wells, R., Bukry, D., Friedman, R., Pyle, D., Duncan, R., Haeussler, P., & Wooden, J. (2014). Geologic history of Siletzia, a large igneous province in the Oregon and Washington Coast Range: Correlation to the geomagnetic polarity time scale and implications for a long-lived Yellowstone hotspot. *Geosphere*, 10(4), 692-719.

Wells, R. E., Blakely, R. J., Wech, A. G., McCrory, P. A., & Michael, A. (2017). Cascadia subduction tremor muted by crustal faults. *Geology*, *45*(6), 515-518.

Wilgus, J., Jiang, C., & Schmandt, B. (2020). A middle crustal channel of radial anisotropy beneath the northeastern Basin and range. *Tectonics*, *39*(7), e2020TC006140.

White, M. C., Fang, H., Nakata, N., & Ben-Zion, Y. (2020). PyKonal: a Python package for solving the eikonal equation in spherical and Cartesian coordinates using the fast marching method. *Seismological Research Letters*, *91*(4), 2378-2389.

Williams, D. L., & Finn, C. (1987). Evidence for a shallow pluton beneath the Goat Rocks Wilderness, Washington, from gravity and magnetic data. *Journal of Geophysical Research: Solid Earth*, 92(B6), 4867-4880.

Xie, J., Ritzwoller, M. H., Brownlee, S. J., & Hacker, B. R. (2015). Inferring the oriented elastic tensor from surface wave observations: preliminary application across the western United States. *Geophysical Journal International*, 201(2), 996-1021.